ADVANCED ELECTRONIC MATERIALS Open Access
www.advelectronicmat.de

Compositional Engineering of Monocrystalline Metal Halide Perovskite Memristors for Multistate Non-Volatile Operation

Ismael Fernandez-Guillen, Miriam Minguez-Avellan, Clara A. Aranda, Pedro Atienzar, Rafael Abargues,* Teresa S. Ripolles, and Pablo P. Boix**

Metal halide perovskite (MHP) memristors hold great promise for next-generation memory and neuromorphic computing. However, challenges such as stability and endurance hinder both their performance and a deeper understanding of their working mechanisms. Advances in thin monocrystalline MHP memristors have demonstrated improved endurance due to the absence of grain boundaries, which makes them an ideal platform for systematically identifying key factors influencing device performance. Thus, evaluating the compositional effects on monocrystalline MHP memristors within a consistent device architecture serves as a powerful approach to deepen understanding of the system and guide the development of application-oriented devices. This strategy is used to fabricate the first memristor based on a mixed-halide thin perovskite monocrystal, which enables multistate non-volatile memristive operation. Furthermore, precise compositional engineering allows control over defect density, which affects the materials' ionic properties and determines key device performance parameters. This study unlocks multistate properties in non-volatile memristors and provides critical insights into defect density effects, paving the way for high-density storage in neuromorphic computing.

1. Introduction

The increasing demand for data computing and the associated power consumption highlight the necessity to explore new technologies utilizing innovative materials that can overcome additional challenges such as the von Neumann bottleneck or Moore's law limitations.[1,2] In this scenario, metal halide perovskites (MHPs) emerge as promising candidates to tackle these questions, due to the significant potential of these materials in advancing the next generation of data computing.[3]

MHPs refer to a family of semiconductors that can offer energy-efficient performance and cost-effective fabrication. Their optoelectronic properties, such as long diffusion length, high defect tolerance, tunable band gap, and high absorption coefficient,[4–6] positioned them as ideal candidates for technologies like lasers,[7] LEDs,[8] and especially solar cells.[9] In their primary niche application, solar cells, MHPs achieve power conversion efficiencies exceeding 26%.[10] However, unlike conventional semiconductors, they present a dual electronic-ionic nature, which is evident in phenomena such as hysteresis in current–voltage curves.[11] While some efforts have been addressed to suppress the impact of ion mobility,[12] this ionic nature can be exploited to develop a new generation of resistive switching technologies.[13]

Resistive switching (RS) memory devices, also known as memristors, are inspired by neural synapses and are being explored as a foundation for next-generation computing technologies.[14] In these systems, information is typically encoded through transitions between a high resistance state (HRS) and a low resistance state (LRS) induced by an external voltage stimulus Among their most promising applications is the development of resistive random-access memories (RRAMs), which offer non-volatile data storage capabilities, retaining information even when powered off.[15,16]

Beyond binary switching, RRAMs are also capable of operating in multistate mode, where devices can exhibit multiple stable resistance levels rather than just two. These multistate memristors are particularly attractive because they allow for higher data storage density and the implementation of

I. Fernandez-Guillen, M. Minguez-Avellan, R. Abargues, T. S. Ripolles
Institute of Materials Science of the University of Valencia
Paterna 46980, Spain
E-mail: ferguis@uv.es; rafael.abargues@uv.es

C. A. Aranda
Department of Physical, Chemical, and Natural Systems
University Pablo de Olavide
Seville 41013, Spain

P. Atienzar, P. P. Boix
Instituto de Tecnología Química (Universitat Politècnica de València – Consejo Superior de Investigaciones Científicas)
Av. Los Naranjos, s/n, Valencia 46022, Spain
E-mail: Pablo.P.Boix@itq.upv.es

The ORCID identification number(s) for the author(s) of this article can be found under https://doi.org/10.1002/aelm.202500494

DOI: 10.1002/aelm.202500494

analog signal processing, essential for emerging paradigms such as neuromorphic computing.[15,17] In such systems, the gradual modulation of resistance states can emulate synaptic weight changes, supporting more sophisticated and energy-efficient learning algorithms.[17,18] However, few multistate RRAM devices based on perovskite materials have been reported, and the mechanisms underlying multistate behavior in such devices are still not fully understood.[19,20,21]

The excellent synergy between the requirements for ideal RS memory devices and the MHPs properties, strongly defined by their ionic mobility, positions this material family as a highly promising platform for next-generation RS technologies. Since the first reports of RS behavior in MHP-based memristors, RRAM devices using MHPs have shown remarkable progress in both performance and versatility, confirming their potential in advanced memory applications.[14] Several formulations of MHPs, including polycrystalline films, nanocrystals, and thin monocrystals, have been explored to optimize the device performance. Each of these systems presents unique complexities, and the limited understanding of the fundamental processes that drive RS behavior in MHPs remains a significant hurdle in their development. Due to the intricate ionic-electronic dynamics involved, the exact mechanisms of RS are still under debate.[22,23] Current literature primarily discusses two mechanisms: the electrochemical metallization mechanism (ECM), driven by metal cations,[24] and the valence change mechanism (VCM), which relies on halide vacancies.[25] While conclusive evidence for either mechanism is still pending, advancing our understanding of these processes is likely essential for the progress of multistate device technology. Additional challenges arise from the inherent characteristics of MHPs and the unique properties of each system. Notably, material instability presents critical issues that directly impact essential parameters like the endurance of RS devices. For instance, polycrystalline MHPs offer scalability but are susceptible to degradation at grain boundaries,[26] while nanocrystals provide enhanced tunability but suffer from increased surface reactivity,[27] adding further sources of instability. Alternatively, thin perovskite monocrystals have demonstrated to enhance memristor endurance and stability by reducing grain boundaries and defects,[15] making monocrystal materials an ideal approach to developing memristors despite the most precise synthesis conditions.

In this work, we perform a comprehensive comparison of three single-halide MHP monocrystals using a consistent device architecture. This systematic analysis is carried out with the goal of identifying which halide composition provides the most favorable properties for memristive applications. Additionally, we extend our analysis by developing thin monocrystalline memristors with mixed halide perovskites to better understand how the halide composition influences memristor properties. We confirm that different halide compositions in thin monocrystalline forms can serve as a tool to modulate defect density within the material,[28,29] thereby directly impacting the mobility of vacancies and ions, as previously reported.[28–30] Here, we demonstrate that defect density directly affects the key properties of memristor devices. Key performance parameters, such as high-to-low resistance state (HRS/LRS) ratio and endurance, can be significantly improved by reducing defect density in the active material. Notably, our results suggest that the emergence of multistate behavior in RRAM memristors is directly influenced by the defect density in MHPs, in conjunction with the effects introduced by mixed-halide compositions, paving the way for a new generation of memristors with high-density data storage and neuromorphic processing capabilities.

2. Results and Discussion

2.1. Structural and Optical Characterization

The confined inverse temperature crystallization method[31] is an effective approach to grow thin monocrystals. These MHP monocrystals, with surface areas exceeding tens of square millimeters and thicknesses in the micrometer range, are ideal for fabricating devices where efficient charge extraction or injection is critical, such as solar cells or memristors.[32,33] The control of the initial precursor solution, as detailed in the experimental section, enables the growth of $MAPbX_3$ monocrystals, where X refers to chloride, bromide, and iodide, and two mixed halide perovskite compounds, $MAPb(Br_{0.8}Cl_{0.2})_3$ and $MAPb(Br_{0.9}I_{0.1})_3$. The lack of reports of thin monocrystals with such mixed halide compositions makes it essential to confirm their properties and structure. Special attention should be paid to ensuring that the halide ratio in the final material accurately reflects the nominal composition.

X-ray diffraction (XRD) patterns of the prepared crystals, **Figure 1a**, show sharp and intense XRD reflections along (100) and (200) planes, confirming the presence of a highly crystalline perovskite cubic phase in the case of $MAPbCl_3$ and $MAPbBr_3$. Regarding $MAPbI_3$, the abrupt reflections corresponding to the (200) and (400) planes confirm the high crystallinity of the samples.[34,35] The (100) peak of $MAPb(Br_{0.8}Cl_{0.2})_3$ shifts by 0.2° to higher angles compared to $MAPbBr_3$, while the same peak in $MAPb(Br_{0.9}I_{0.1})_3$ shifts by 0.09° to smaller angles (inset Figure 1a). Such displacements are consistent with Vegard's law,[36,37] partially substituting the smaller Br^- anion with the larger I^- anion expands the lattice constant, whereas replacing Br^- with the smaller Cl^- anion results in further contraction.[38] Energy dispersive X-ray (EDX) analysis (Figure S1, Supporting Information) confirms that the actual compositions are $MAPb(Br_{0.8}Cl_{0.2})_3$ and $MAPb(Br_{0.9}I_{0.1})_3$, which closely match their respective nominal compositions. Each EDX analysis is linked to its corresponding top-view SEM image in Figure S1 (Supporting Information). The thickness of the different monocrystals is measured by profilometry, Figure S2 (Supporting Information), confirming a thickness of 20–25 μm in all cases.

Photoluminescence (PL) (Figure 1b) can be used as a tool for evaluating the qualitative optoelectrical quality and composition of the crystals. The pure halide compositions, $MAPbCl_3$, $MAPbBr_3$, and $MAPbI_3$, exhibit sharp and narrow emission peaks, with maximum emission wavelengths at 395, 533, and 760 nm, respectively, in accordance with previous literature reports.[39,40] In contrast, the mixed halide monocrystals, $MAPb(Br_{0.9}I_{0.1})_3$ and $MAPb(Br_{0.8}Cl_{0.2})_3$, display maximum emission peaks at 510 and 728 nm, respectively. Notably, no phase segregation is observed during the measurements, which is a common issue in mixed halide compositions, particularly in their polycrystalline forms.[28,41,42] Additional morphological characterization, including representative top-view and cross-sectional

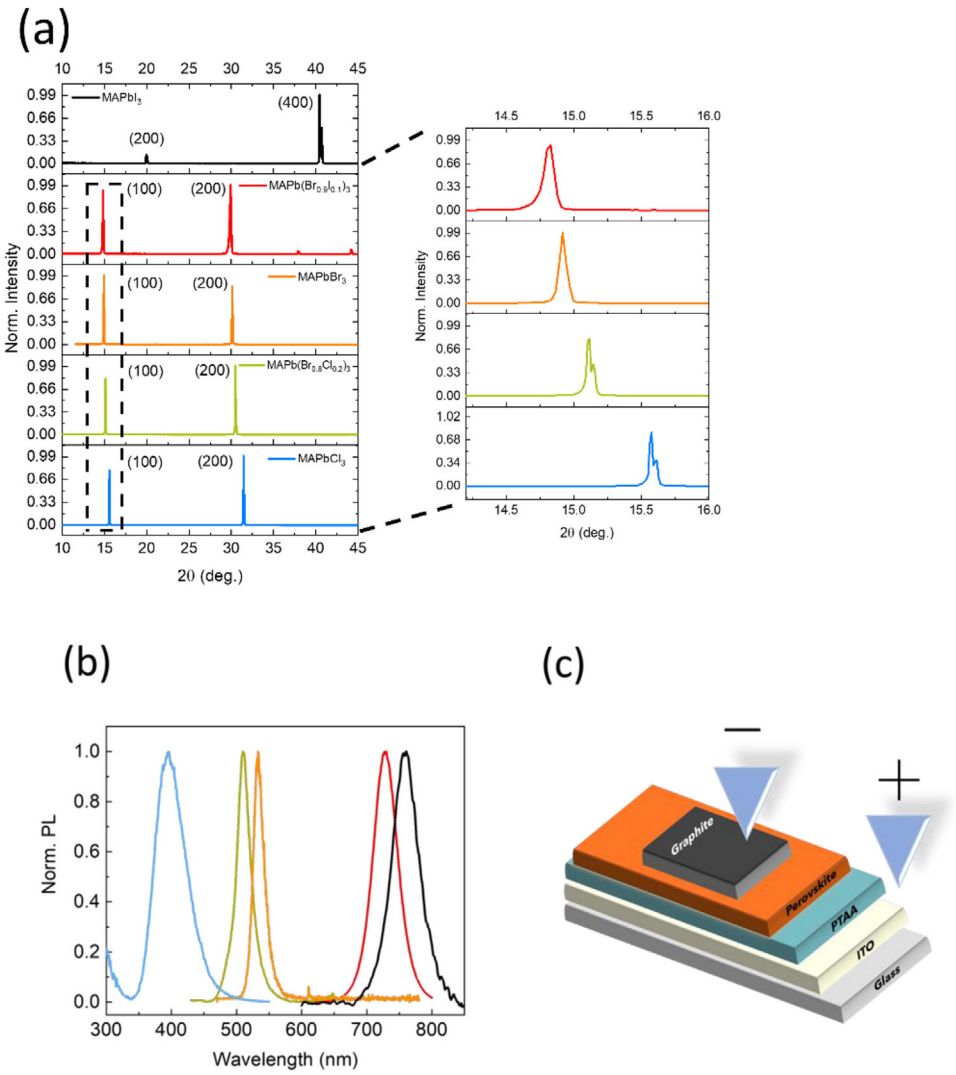

Figure 1. a) XRD patterns, b) PL emission of $MAPbCl_3$ (blue line), $MAPbBr_3$ (orange line), $MAPbI_3$ (black line), $MAPb(Br_{0.9}I_{0.1})_3$ (red line), and $MAPb(Br_{0.8}Cl_{0.2})_3$ (green line) thin monocrystalline perovskites, and c) device architecture of the memristor devices.

images of the monocrystal, reveals a smooth, pinhole-free surface with a thickness of ≈20 μm, as shown in Figure S3 (Supporting Information). Optical top-view images of the different compositions are also presented in Figure S3 (Supporting Information), showing a surface area from ≈4 to 8 mm^2. Note that $MAPbCl_3$ does not emit in the visible region and is therefore not included in the optical images, however, a top-view SEM image of the $MAPbCl_3$ composition is included in Figure S3 (Supporting Information).

2.2. Characterization of Monocrystalline Pure Halide Memristor Devices

The MHP monocrystals were implemented in memristor devices in a simple architecture, as represented in Figure 1c, where Poly[bis(4-phenyl)(2,4,6-trimethylphenyl)amine, PTAA, is selected as a buffer layer, and graphite is used as a low-reactive electrode. PTAA serves multiple purposes: i) to enhance interfacial stability and suppress deleterious reactions between the perovskite and the bottom electrode, ii) to facilitate crystal growth due to its hydrophobic nature, which promotes halide diffusion during crystallization, and iii) to potentially assist in hole transport, given that PTAA is a well-known hole transport material. Graphite is selected as the electrode due to its high electrical conductivity and chemical inertness. Due to their improved stability resulting from the suppression of grain boundaries, monocrystalline perovskites are an ideal platform to accomplish high-endurance memristor devices. This enables a more exhaustive analysis of the device's working mechanisms. Thus, here we extend the study to the different halide compositions to better understand the dynamics of the RS mechanisms.

Cyclic-voltammetry measurements of the pure halide memristors (see **Figure 2a**) were performed to compare the behavior of crystals based on different halides. The $MAPbCl_3$ memristor exhibited the highest set voltage (at which the device transitions

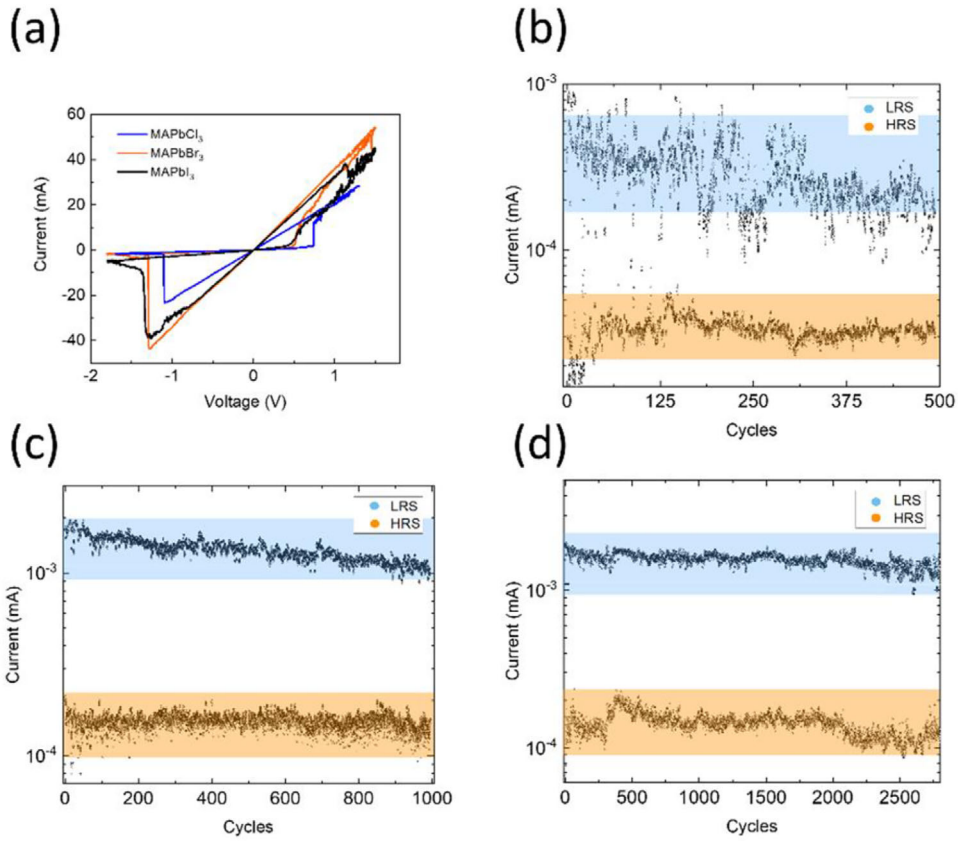

Figure 2. a) Cyclic-voltammetry of $MAPbCl_3$ (blue line), $MAPbBr_3$ (orange line), and $MAPbI_3$ (black line) monocrystal memristor devices. Endurance performance test conducted by applying cyclic sweep voltages in the sequence of +1.5, +0.07, −2, and +0.07 V on b) $MAPbCl_3$, c) $MAPbBr_3$, and d) $MAPbI_3$ monocrystal memristor devices.

from LRS to HRS) at 0.75 V, and the lower reset voltage (transition from HRS to LRS) at −1.1 V. In contrast, the $MAPbBr_3$ memristor showed a set voltage of 0.52 V and a reset voltage of −1.29 V. Similarly, the $MAPbI_3$ memristor demonstrated a set voltage of 0.43 V and a reset voltage of −1.34 V. It is worth remarking that the transitions from LRS to HRS (Figure 2a) occur abruptly for the three pure halide compositions, and no clear correlation is observed between the set/reset potentials and the materials' bandgap. Despite certain variation in the absolute potential values for set and reset voltages (Figure S4, Supporting Information), the samples maintain the abrupt transition (Figure 2a).

Additionally, an endurance test was conducted to examine the stability of the memristors. A sequence of voltage steps was applied in the following order: +1.5, +0.07, −2, and finally +0.07 V. Specifically, +0.07 V was used as the read voltage, +1.5 V as the set voltage, and −2 V as the reset voltage. Figure 2b presents the endurance test results for the $MAPbCl_3$ device. A significant dispersion in the LRS is clearly observed during the measurement, and the device eventually fails after 500 cycles. The LRS/HRS ratio remains close to 100 for the first 125 cycles, but gradually stabilizes at ≈10 for the rest of the measurement. In contrast, the endurance analysis of $MAPbBr_3$ (see Figure 2c) shows no significant dispersion over 1000 cycles, maintaining an LRS/HRS ratio exceeding 10. The $MAPbI_3$ endurance test, displayed in Figure 2d, demonstrates one of the highest endurance values reported in the literature, with more than 2800 cycles without significant dispersion, and a stable LRS/HRS ratio above 10. Notably, the endurance performance varies significantly depending on the halide composition, with ≈500 cycles for $MAPbCl_3$, ≈1000 cycles for $MAPbBr_3$, and ≈2800 cycles for $MAPbI_3$.

Long-term retention time of the LRS and the HRS is another key parameter for RRAM devices, as this determines how long the device can reliably store information. To characterize retention times, chronoamperometry is measured in which the current is continuously measured at +0.07 V, the read voltage, for both states, first the LRS and subsequently, the HRS, along 10^4 s. The retention time analysis for $MAPbCl_3$ (Figure S5a, Supporting Information) shows that the LRS/HRS ratio reaches 100 during the first 250 s. However, after this period, the current in the HRS increases from 10 to 100 μA, exhibiting high instability in the HRS. Nevertheless, the LRS remains stable throughout the measurement, achieving a retention time of 3000 s for the Cl-based composition. In contrast, the $MAPbBr_3$ device (Figure S5b, Supporting Information) demonstrates high stability in both LRS and HRS states throughout the entire measurement period of 10^4 s, maintaining an LRS/HRS ratio of 30. Similarly, the $MAPbI_3$ device (Figure S5c, Supporting Information) exhibits a retention time of 10^4 s, with the HRS showing no significant fluctuations, while the LRS decreases slightly over time. Despite this minor variation, the LRS/HRS

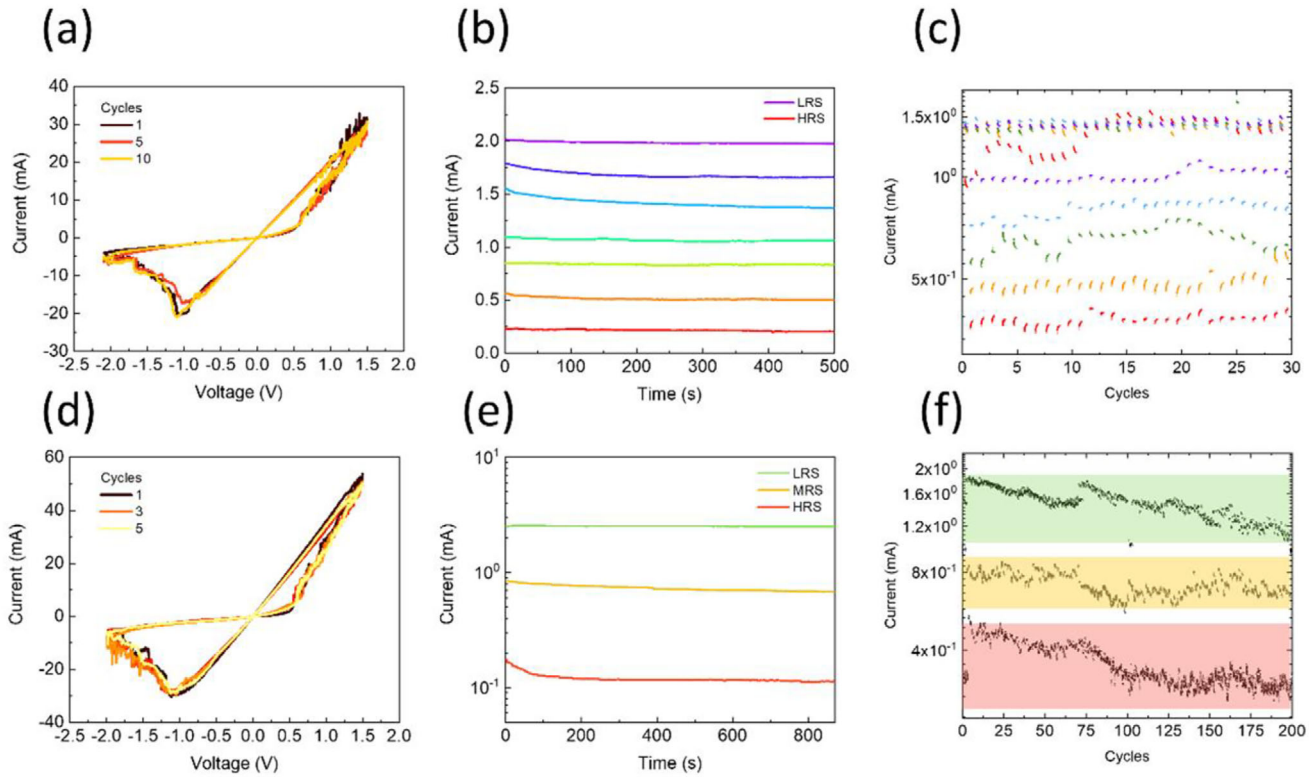

Figure 3. a) Cyclic-voltammetry, b) chronoamperometry, and c) endurance test performance of the $MAPb(Br_{0.9}I_{0.1})_3$ monocrystal memristor device. d) Cyclic-voltammetry, e) chronoamperometry, and f) endurance test performance of the $MAPb(Br_{0.8}Cl_{0.2})_3$ monocrystal memristor device.

ratio remains consistently ≈30 for the entire measurement duration.

2.3. Characterization of Monocrystalline Mixed Halide Memristor Devices

Memristors based on mixed halide perovskite thin monocrystals facilitate a deeper analysis of ionic-electronic dynamics and device mechanisms. The study focuses on $MAPb(Br_{0.9}I_{0.1})_3$ and $MAPb(Br_{0.8}Cl_{0.2})_3$ memristor devices. **Figure 3a** illustrates the performance of the $MAPb(Br_{0.9}I_{0.1})_3$ device during cyclic-voltammetry measurements, showing a set voltage of +0.55 V. Notably, the reset voltage transition is gradual, beginning at −1 V and progressing up to −2 V, at which the device fully transitions to the HRS. This gradual transition, unlike the abrupt switching observed in pure halide memristors (Figure 2a), enables the operation of multistate devices using mixed halide monocrystalline perovskites. By selecting a reset voltage within the transition range, one can determine the HRS resistance, allowing for multiple resistance states.

Figure 3b displays a retention time test of the $MAPb(Br_{0.9}I_{0.1})_3$ device, where the read voltage is fixed to +0.07 V. The HRS obtained at −2 V, with a response of 0.2 mA. The LRS set by a +1.5 V and defined by a 2 mA response. Intermediate states are achieved when the reset voltage is set within the range of −2 V (corresponding to the HRS) and −1.1 V. Up to seven clearly differentiable states can be achieved by changing the reset voltages. The retention time reaches 500 s for each state, for a total retention time of 3500 s. Nevertheless, to assess the device's practical application, it is crucial to maintain the multistate configuration during endurance testing without any dispersion among the states. The dispersion in endurance measurements of a memristor causes variations in resistance states, leading to read errors and unreliable data processing. In neuromorphic computing, this variability can cause weight drift, affecting neural network performance, while in memory applications, it shortens device lifespan and requires error correction mechanisms to maintain reliability.[43,44]

The endurance test for the $MAPb(Br_{0.9}I_{0.1})_3$ device (see Figure 3c) was performed using a specific sequence of voltage steps, starting at a set voltage of +1.5 V, followed by +0.07 V, then a reset voltage that varied between −2, −1.8, −1.5, −1.3 and −1.1 V, and finally returning to the reading voltage of +0.07 V. For clarity, this sequence is visually represented in Figure S6 (Supporting Information). The sequence begins with a reset voltage of −2 V, followed by −1.8 V, and gradually decreases to -1.1 V. At this point, the entire sequence is repeated 30 times for each reset voltage. As shown in Figure 3b, up to six distinct states are achieved during 30 cycles for each voltage, resulting in a total of 150 cycles of stability. As mentioned above, although seven states are achieved during the retention test, the functional application is defined by six states without dispersion, which is performed in the endurance test.

The cyclic-voltammetry of the $MAPb(Br_{0.8}Cl_{0.2})_3$ device (Figure 3d) is similar to that of $MAPb(Br_{0.9}I_{0.1})_3$. The set voltage

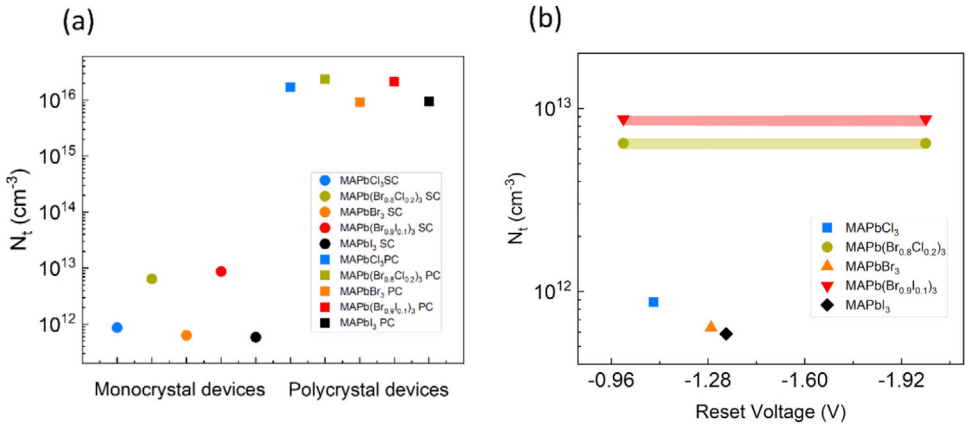

Figure 4. a) Defect density of monocrystal (circle points) and polycrystal (square points) memristor devices. b) Reset the voltage dependence of monocrystal devices with respect to defect density.

occurs at +0.55 V, and the reset voltage ranges between −1 and −2 when the device fully reaches the HRS. Figure 3e displays the retention time for three different states obtained within that range where the read voltage is +0.07 V. The three states remain stable for 900 s each one with an LRS/HRS ratio of 30 between the extremes. The endurance test (see Figure 3f) was performed using a specific sequence of voltage steps, starting at a set voltage of +1.5 V, followed by a read voltage of +0.07 V, then a reset voltage that varied between −2 and −1.5 V, and finally returning to +0.07 V. In the case of MAPb($Br_{0.8}Cl_{.0.2}$)$_3$ devices, three different states can be achieved, reaching 200 cycles for each one. While the three states are completely differentiable, the high dispersion observed during the endurance cycles prevents the achievement of additional states, as observed in the MAPb($Br_{0.9}I_{0.1}$)$_3$ device. Up to 9 states can be distinguished in the retention test for MAPb($Br_{0.8}Cl_{0.2}$)$_3$, Figure S7 (Supporting Information), but these must be differentiated during the endurance test to enable a functional multistate device, as mentioned above.

2.4. Switching Mechanism

With these results, the use of mixed halide perovskite monocrystal devices instead of pure halide ones unlocks new possibilities for the fabrication of multistate memristor devices. Considering this comprehensive range of compositions, the relation between the defect density of each perovskite and the dynamics of the memristive mechanism can be used to gain insights on their working mechanisms. Here, it is worth highlighting that a low-reactivity electrode, such as graphite, is used to mitigate the role of the electrode in the operation of the device. Moreover, the devices can be operated without such an electrode, with direct contact from the measuring tip on the surface, see the cyclic voltammetry shown in Figure S8 (Supporting Information). There are no qualitative changes in the behavior of the device when graphite is not used. This fact discards the relevant role of graphite in the memristive behavior.

The space charge limited current (SCLC) regime of hole-only devices was measured for all analyzed monocrystalline perovskite compositions (Figure S9, Supporting Information) and compared to their polycrystalline counterparts (Figure S10, Supporting Information). SCLC measurement was conducted using a symmetric sandwiched structure, using poly[bis(4-phenyl)(2,4,6-trimethylphenyl)amine)] (PTAA) as the selective layer, while avoiding graphite as the contact electrode. The most common approach to determine the trap density based on the so-called trap-limit voltage:[45,46]

$$V_{TFL} = \frac{e n_t L^2}{2\varepsilon\varepsilon_0} \quad (1)$$

where, V_{TFL} is the voltage of trap filling; e is the electronic charge; n_t corresponds to the density of trapped carriers; L is the thickness of the active material; ε is its dielectric constant; and ε_0 corresponds to vacuum permittivity. The obtained values for the monocrystal and polycrystal devices are summarized in Tables S1 and S2 (Supporting Information), respectively, and represented in **Figure 4a**. In the case of monocrystalline devices, the use of mixed halide compositions (10^{13} cm^{-3}) increases the defect density by one order of magnitude compared to pure halide memristors (10^{12} cm^{-3}). Regarding polycrystalline devices, their defect density is ≈10^{16} cm^{-3} for the single halide compositions, and the mixed halide compositions exhibit values slightly higher yet within the same order of magnitude. All the defect density values of polycrystalline perovskite and pure halide monocrystalline perovskite are in agreement with those reported in the literature.[47] Mixed halide perovskite monocrystals have been studied far less extensively, and our results suggest that incorporating mixed halides may increase the defect density in these materials.[28]

Defect density plays a crucial role in determining the ionic properties of crystals. Therefore, it is important to assess its impact on key parameters of memristive devices. Figure 4b displays the reset voltage of the monocrystalline memristive devices as a function of the materials' defect density. $MAPbI_3$ exhibits the lowest defect density and the most negative reset voltage of the pure halide devices. $MAPbBr_3$ displays marginally more defect density and lower reset voltage than $MAPbI_3$. Following that trend, $MAPbCl_3$ presents a slightly higher defect density, and the lowest reset voltage compared to pure halide

devices. As mentioned above, memristive devices based on mixed halide monocrystalline compositions show a gradual reset. In both cases, the reset voltage starts approximately at −1 V and finishes at −2 V, although $MAPb(Br_{0.8}Cl_{0.2})_3$ exhibits slightly lower defect density than $MAPb(Br_{0.9}I_{0.1})_3$ composition. We tentatively relate the gradual reset to the higher defect density, almost one order of magnitude compared to single halide monocrystalline devices.

Figure S11 (Supporting Information) compares the monocrystalline devices' cyclic voltammetry with their polycrystalline counterpart. Remarkably, the HRS in polycrystalline devices is close to the LRS in all cases of monocrystalline devices, exhibiting an LRS/HRS ratio of 2 for the polycrystalline memristors, contrasting with a ratio of 30 for monocrystal devices. A clear correlation between a high LRS/HRS ratio and low defect density is evident when comparing the performance of monocrystal and polycrystal devices. Lower defect densities of monocrystals translate to an LRS/HRS ratio of ≈10. In contrast, polycrystalline devices, with four orders of magnitude higher defect densities, present an LRS/HRS ratio of 2.

Finally, the electroforming voltage (visible in the electroforming cyclic voltammetry processes, represented in Figure S12, Supporting Information) also displays a strong dependence on the material's defect density. In the case of pure halide monocrystals, the electroforming voltage occurs at ≈4.5 V, while that of mixed halide monocrystals is ≈2.5 V. Regarding the polycrystalline devices, their electroforming voltage is ≈1.2 V.

The effects of defect density on various memristive device parameters can be understood in terms of its correlation with lower migration energy.[30,48] The regulation of ionic mobility by defect density directly impacts device performance. Our results suggest that memristors with optimal properties exhibit low defect densities ($<10^{-12}$ cm^{-3}), while high-quality multistate memristors can be achieved at 10^{-13} cm^{-3}. In contrast, higher defect densities obtained with polycrystalline films, $>10^{-15}$ cm^{-3}, degrade device performance, reducing the LRS/HRS ratio by more than one order of magnitude compared with lower-defect-density counterparts.

3. Conclusion

In summary, the performance of monocrystalline MHP memristors is strongly influenced by halide composition. $MAPbCl_3$ exhibits the poorest performance, with an endurance of 500 cycles, an HRS/LRS ratio of 10, and a retention time of 3000 s. In contrast, $MAPbBr_3$ demonstrates stable performance over 1000 cycles, with an LRS/HRS ratio of up to 30 and a retention time of 10^4 s. $MAPbI_3$, offers the best performance for monocrystalline memristors, withstanding 2500 cycles while maintaining a consistent HRS/LRS ratio throughout 10^4 s of retention.

Building on these observations, the development of mixed-halide thin monocrystals enables gradual resistive switching behavior, making them well-suited for multi-state device applications. Specifically, $MAPb(Br_{0.9}I_{0.1})_3$ composition exhibits superior multistate performance, achieving six distinct conductance states during the endurance test, whereas $MAPb(Br_{0.8}Cl_{0.2})_3$ shows only three.

The control over defect density critically affects device characteristics, such as the LRS/HRS ratio, as evidenced by comparing monocrystal and polycrystal devices. This indicates that multistate RRAM memristors can be closely linked to the defect density of the MHPs, particularly when combined with the use of mixed-halide compositions, without implying that defect density is the only determining factor.

Overall, this work advances the understanding and design of high-performance, multistate memristors for next-generation, high-density data storage applications.

4. Experimental Section

Materials: Lead chloride ($PbCl_2$), lead bromide ($PbBr_2$), and lead iodine (PbI_2) were purchased from TCI. Methylammonium chloride (CH_3NH_3Cl, MACl), methylammonium bromide (CH_3NH_3Br, MABr), and methylammonium iodine (CH_3NH_3I, MAI) were purchased from GreatCell. Polytriarylamine (PTAA) was purchased from Ossila. N, N-dimethylformamide (DMF) and dimethyl sulfoxide (DMSO) were purchased from Thermo Scientific. γ-Butyrolactone (GBL) was purchased from TCI. Toluene was purchased from VWR. Graphite spray was purchased from RS. All the reagents were directly used without any further purification.

Device Fabrication Process—Monocrystal Memristor Devices: The precursor solutions for 1 M $MAPbX_3$ (X = Cl, Br, I) perovskites were prepared by dissolving a 1:1 molar ratio of PbX_2 and MAX in an appropriate solvent. For the $MAPbCl_3$ precursor solution, the precursors $PbCl_2$ and MACl were solved by DMF: DMSO (1:1, vol:vol), followed by vigorous shaking to ensure complete dissolution. The $MAPbBr_3$ precursor solution was prepared by dissolving $PbBr_2$ and MABr in DMF under vigorous shaking. Similarly, the $MAPbI_3$ precursor solution was prepared by dissolving PbI_2 and MAI in GBL under the same stirring conditions. The $MAPb(Br_{0.8}Cl_{0.2})_3$ precursor solution was prepared by mixing the pure solutions $MAPbCl_3$:$MAPbBr_3$ in a 1:4 volume ratio. The $MAPb(Br_{0.9}I_{0.1})_3$ precursor solution was prepared by mixing the pure solutions of $MAPbI_3$:$MAPbBr_3$ in a 1:4 volume ratio. All the solutions were filtered using a 0.2 µm PTFE syringe filter before deposition.

Glass/ITO substrates were cleaned sequentially using acetone, detergent, deionized water, and absolute ethanol, with each step performed in an ultrasonic bath for 10 min. After drying with air flow, the substrates were treated in a UV-O_3 cleaner for 20 min. Subsequently, 40 µL of the prepared PTAA solution (2 mg mL^{-1} dissolved in toluene) was deposited onto the ITO substrate by spin-coater at 4000 rpm for 30 s under ambient conditions. Immediately, the substrates were annealed at 100 °C for 10 min.

The space-confined inverse temperature crystallization method was used for growing thin monocrystals. The temperature was gradually increased from 25 to 80 °C at a rate of 12 °C h^{-1} for all the compositions except $MAPbI_3$. For $MAPbI_3$, the temperature ramp started from 50 °C and increased to 120 °C at a rate of 8 °C h^{-1}. The substrates were held at 80 and 120 °C, respectively for 24 h. After cooling at room temperature, the substrates were separated with a blade. Finally, the graphite electrodes were added on top of the perovskite monocrystals by depositing 10 µL of the graphite solution with a micropipette. The solution evaporates in 60 s after deposition, approximately, forming a solid graphite that acts as an electrode. It is important to note that the device is fabricated outside of the glovebox.

Device Fabrication Process—Polycrystal Memristor Devices: All solutions used for preparing polycrystalline perovskites were the same as those used for synthesizing monocrystalline perovskites. The solutions were added to the ITO substrates treated with PTAA, as previously described. Subsequently, the solutions were spin-coated with a sequence of 1000 rpm for 10 s and 4000 rpm for 40 s, adding 300 µL of toluene at 12 s of the second step for all the compositions except $MAPbI_3$, whose toluene addition time is 22 s. Then, the device is annealed for 30 min at 100 °C. Finally, the graphite electrodes were deposited on the $MAPbX_3$. All the device experimental processes were fabricated inside a glovebox.

Characterization: Profilometer measurements were performed using a Dektak 150 Surface Profiler from Veeco equipment. The crystalline structure was assessed by XRD collected on a Bruker D8 Advanced X-ray diffractometer with copper K_α radiation (l = 1.5418 A°) and a scan rate of 5° min^{-1} for 2θ angles ranging from 12° to 40°. EDX analysis were performed by a S-4800 instrument from HITACHI (Tokyo, Japan) operating at 10 kV. Electrical characterizations were measured using a Gamry interface 1010E. Photoluminescence measurements on the monocrystals were carried out using an inverted microscope, Nikon (Tokyo, Japan) Ti2-U, equipped with a XY motorized stage. The emission signal was transmitted through optical fibers to an Edinburgh Instruments (Livingston, UK) FLS1100 spectrofluorometer, which was coupled to a cooled photomultiplier (PMT-980). The measurements were performed at room temperature, utilizing a 405 nm excitation wavelength provided by a picosecond (ps) laser diode incorporated into the microscope.

Supporting Information

Supporting Information is available from the Wiley Online Library or from the author.

Acknowledgements

This study forms part of the Advanced Materials programme and was supported by MCIN with funding from European Union NextGenerationEU (PRTR-C17.I1) and by the Generalitat Valenciana (code MFA/2022/040/007). The work was partially funded by MCIN/AEI through project TED2021-131600B-C32. P.P.B. and T.S.R. thank Generalitat Valenciana for the funding via Pla Gent-T (grants CIDEGENT/2021/044 and ESGENT/010/2024). These results are part of the grant CNS2023-144270 funded by MICIU/AEI/10.13039/501100011033 and by European Union NextGenerationEU/PRTR. C.A.A. was supported by the Margarita Salas postdoctoral contract MGS/2021/24(UP2021-021) financed by the European Union-NextGenerationEU.

Conflict of Interest

The authors declare no conflict of interest.

Data Availability Statement

The data that support the findings of this study are available from the corresponding author upon reasonable request.

Keywords

memristors, mixed halides, monocrystals, multistates, perovskite

Received: August 4, 2025
Revised: October 19, 2025
Published online: November 19, 2025

[1] H. Rong, H. Zhang, S. Xiao, C. Li, C. Hu, *Renew. Sustain. Energy Rev.* **2016**, *58*, 674.
[2] H. S. P. Wong, S. Salahuddin, *Nat. Nanotechnol.* **2015**, *10*, 191.
[3] H. Seok, D. Lee, S. Son, H. Choi, G. Kim, T. Kim, *Adv. Electron. Mater.* **2024**, *10*, 2300839.
[4] U. C. Gupta, *Inf. Syst. Manag.* **1992**, *9*, 28.
[5] I. Fernandez-Guillen, V. S. Chirvony, M. Krečmarová, G. Muñoz-Matutano, J. Ortiga-Fibla, A. Cros, N. Garro, J. F. Sánchez-Royo, P. J. Martínez-Pastor, M. C. Asensio, R. Abargues, P. P. Boix, *ACS Photonics* **2023**, *10*, 4151.
[6] M. A. Green, A. Ho-Baillie, H. J. Snaith, *Nat. Photonics* **2014**, *8*, 506.
[7] L. Lei, Q. Dong, K. Gundogdu, F. So, *Adv. Funct. Mater.* **2021**, *31*, 1, https://DOI:10.1002/adfm.202010144
[8] J. Noguera-Gómez, I. Fernández-Guillen, P. F. Betancur, V. S. Chirvony, P. P. Boix, R. Abargues, *Matter* **2022**, *5*, 3541.
[9] N. G. Park, *Mater. Today* **2015**, *18*, 65.
[10] H. Chen, C. Liu, J. Xu, A. Maxwell, W. Zhou, Y. Yang, Q. Zhou, A. S. R. Bati, H. Wan, Z. Wang, L. Zeng, J. Wang, P. Serles, Y. Liu, S. Teale, Y. Liu, M. I. Saidaminov, M. Li, N. Rolston, S. Hoogland, T. Filleter, M. G. Kanatzidis, B. Chen, Z. Ning, E. H. Sargent, *Science* **2024**, *384*, 189.
[11] J. Thiesbrummel, S. Shah, E. Gutierrez-Partida, F. Zu, F. Peña-Camargo, S. Zeiske, J. Diekmann, F. Ye, K. P. Peters, K. O. Brinkmann, P. Caprioglio, A. Dasgupta, S. Seo, F. A. Adeleye, J. Warby, Q. Jeangros, F. Lang, S. Zhang, S. Albrecht, T. Riedl, A. Armin, D. Neher, N. Koch, Y. Wu, V. M. Le Corre, H. Snaith, M. Stolterfoht, *Nat. Energy* **2024**, *9*, 664.
[12] C. A. Aranda, A. O. Alvarez, V. S. Chivrony, C. Das, M. Rai, M. Saliba, *Joule* **2024**, *8*, 241.
[13] C. Zhang, Y. Li, C. Ma, Q. Zhang, *Small Sci.* **2022**, *2*, 2100086.
[14] W. Peixiong, C. Xiang, P. Xiaoxin, J. Bowen, L. Xiaoqing, P. Yanqin, P. Jie, T. Li, D. Jinxia, Z. Jun, W. Hao, *Mater. Today Energy* **2024**, *45*, 101692.
[15] I. Fernandez-Guillen, C. A. Aranda, P. F. Betancur, M. Vallés-Pelarda, C. Momblona, T. S. Ripolles, R. Abargues, P. P. Boix, *Adv. Electron. Mater.* **2024**, *10*, 2300475.
[16] R. A. John, Y. Demirağ, Y. Shynkarenko, Y. Berezovska, N. Ohannessian, M. Payvand, P. Zeng, M. I. Bodnarchuk, F. Krumeich, G. Kara, I. Shorubalko, M. V. Nair, G. A. Cooke, T. Lippert, G. Indiveri, M. V. Kovalenko, *Nat. Commun.* **2022**, *13*, 1, https://DOI:10.1038/s41467-022-29727-1
[17] F. Luo, W. M. Zhong, X. G. Tang, J. Y. Chen, Y. P. Jiang, Q. X. Liu, *Nano Mater. Sci.* **2024**, *6*, 68.
[18] I. H. Im, J. H. Baek, S. J. Kim, J. Kim, S. H. Park, J. Y. Kim, J. J. Yang, H. W. Jang, *Adv. Mater.* **2024**, *36*, 2307334.
[19] J. Cui, X. Fu, H. Zhou, J. Yin, M. Wu, X. Zhang, *Dalt. Trans.* **2021**, *50*, 10365.
[20] J. Xing, C. Zhao, Y. Zou, W. Kong, Z. Yu, Y. Shan, Q. Dong, D. Zhou, W. Yu, C. Guo, *Light Sci. Appl.* **2020**, *9*, 111.
[21] S. Zhai, J. Gong, Y. Feng, Z. Que, W. Mao, X. He, Y. Xie, X. Li, L. Chu, *iScience* **2023**, *26*, 106461.
[22] S. Y. Kim, H. Zhang, J. Rubio-Magnieto, *J. Phys. Chem. Lett.* **2024**, 10087.
[23] B. Li, W. Hui, X. Ran, Y. Xia, F. Xia, L. Chao, Y. Chen, W. Huang, *J. Mater. Chem. C* **2019**, *7*, 7476.
[24] H. L. Park, T. W. Lee, *Org. Electron.* **2021**, *98*, 106301.
[25] J. Yang, F. Zhang, H. M. Xiao, Z. P. Wang, P. Xie, Z. Feng, J. Wang, J. Mao, Y. Zhou, S. T. Han, *ACS Nano* **2022**, *16*, 21324.
[26] S. P. Dunfield, L. Bliss, F. Zhang, J. M. Luther, K. Zhu, M. F. A. M. van Hest, M. O. Reese, J. J. Berry, *Adv. Energy Mater.* **2020**, *10*, 1904054.
[27] D. Yang, X. Li, H. Zeng, *Adv. Mater. Interfaces* **2018**, *5*, 1, https://DOI:10.1002/adma.201803515
[28] A. J. Barker, A. Sadhanala, F. Deschler, M. Gandini, S. P. Senanayak, P. M. Pearce, E. Mosconi, A. J. Pearson, Y. Wu, A. R. Srimath Kandada, T. Leijtens, F. De Angelis, S. E. Dutton, A. Petrozza, R. H. Friend, *ACS Energy Lett.* **2017**, *2*, 1416.
[29] M. Ledinsky, A. Vlk, T. Schonfeldova, J. Holovsky, E. Aydin, H. X. Dang, Z. Hajkova, L. Landova, J. Valenta, A. Fejfar, S. de Wolf, *J. Phys. Chem. C* **2020**, *124*, 27333.
[30] H. Zai, Y. Ma, Q. Chen, H. Zhou, *J. Energy Chem.* **2021**, *63*, 528.

[31] Y.-X. Chen, Q.-Q. Ge, Y. Shi, J. Liu, D.-J. Xue, J.-Y. Ma, J. Ding, H.-J. Yan, J.-S. Hu, L.-J. Wan, *J. Am. Chem. Soc.* **2016**, *138*, 16196.
[32] S. Shrestha, X. Li, H. Tsai, C. H. Hou, H. H. Huang, D. Ghosh, J. J. Shyue, L. Wang, S. Tretiak, X. Ma, W. Nie, *Chem* **2022**, *8*, 1107.
[33] B. Turedi, M. N. Lintangpradipto, O. J. Sandberg, A. Yazmaciyan, G. J. Matt, A. Y. Alsalloum, K. Almasabi, K. Sakhatskyi, S. Yakunin, X. Zheng, R. Naphade, S. Nematulloev, V. Yeddu, D. Baran, A. Armin, M. I. Saidaminov, M. V. Kovalenko, O. F. Mohammed, O. M. Bakr, *Adv. Mater.* **2022**, *34*, 2202390.
[34] J. Zhang, K. Wang, Q. Yao, Y. Yuan, J. Ding, W. Zhang, H. Sun, C. Shang, C. Li, T. Zhou, S. Pang, *ACS Appl. Mater. Interfaces* **2021**, *13*, 29827.
[35] Z. Chen, B. Turedi, A. Y. Alsalloum, C. Yang, X. Zheng, I. Gereige, A. Alsaggaf, O. F. Mohammed, O. M. Bakr, *ACS Energy Lett.* **2019**, *4*, 1258.
[36] Y. Nakamura, N. Shibayama, A. Hori, T. Matsushita, H. Segawa, T. Kondo, *Inorg. Chem.* **2020**, *59*, 6709.
[37] A. Liang, J. Gonzalez-Platas, R. Turnbull, C. Popescu, I. Fernandez-Guillen, R. Abargues, P. P. Boix, L. T. Shi, D. Errandonea, *J. Am. Chem. Soc.* **2022**, *144*, 20099.
[38] S. Y. Kim, H. C. Lee, Y. Nam, Y. Yun, S. H. Lee, D. H. Kim, J. H. Noh, J. H. Lee, D. H. Kim, S. Lee, Y. W. Heo, *Acta Mater.* **2019**, *181*, 460.
[39] W. Wang, J. Su, L. Zhang, Y. Lei, D. Wang, D. Lu, Y. Bai, *CrystEngComm* **2018**, *20*, 1635.
[40] C. M. Sutter-Fella, Y. Li, M. Amani, J. W. Ager, F. M. Toma, E. Yablonovitch, I. D. Sharp, A. Javey, *Nano Lett.* **2016**, *16*, 800.
[41] A. J. Knight, J. Borchert, R. D. J. Oliver, J. B. Patel, P. G. Radaelli, H. J. Snaith, M. B. Johnston, L. M. Herz, *ACS Energy Lett.* **2021**, *6*, 799.
[42] E. T. Hoke, D. J. Slotcavage, E. R. Dohner, A. R. Bowring, H. I. Karunadasa, M. D. McGehee, *Chem. Sci.* **2015**, *6*, 613.
[43] M. Lanza, R. Waser, D. Ielmini, J. J. Yang, L. Goux, J. Suñe, A. J. Kenyon, A. Mehonic, S. Spiga, V. Rana, S. Wiefels, S. Menzel, I. Valov, M. A. Villena, E. Miranda, X. Jing, F. Campabadal, M. B. Gonzalez, F. Aguirre, F. Palumbo, K. Zhu, J. B. Roldan, F. M. Puglisi, L. Larcher, T. H. Hou, T. Prodromakis, Y. Yang, P. Huang, T. Wan, Y. Chai, et al., *ACS Nano* **2021**, *15*, 17214.
[44] M. Zhao, B. Gao, Y. Xi, F. Xu, H. Wu, H. Qian, *IEEE J. Electron Devices Soc.* **2019**, *7*, 1239.
[45] P. Mark, W. Helfrich, *J. Appl. Phys.* **1962**, *33*, 205.
[46] R. H. Bube, *J. Appl. Phys.* **1962**, *33*, 1733.
[47] J. Siekmann, S. Ravishankar, T. Kirchartz, *ACS Energy Lett.* **2021**, *6*, 3244.
[48] D. Meggiolaro, E. Mosconi, F. De Angelis, *ACS Energy Lett.* **2019**, *4*, 779.